Contents lists available at ScienceDirect

Applied Catalysis B: Environmental

Efficient visible light-induced H_2 production by Au@CdS/TiO$_2$ nanofibers: Synergistic effect of core–shell structured Au@CdS and densely packed TiO$_2$ nanoparticles

Minju Kim [a,1], Young Kwang Kim [b,1], Sang Kyoo Lim [b], Soonhyun Kim [b,*], Su-Il In [a,**]

[a] *Department of Energy Systems Engineering, Daegu Gyeongbuk Institute of Science and Technology (DGIST), Daegu 711-873, Republic of Korea*
[b] *Nano & Bio Research Division, Daegu Gyeongbuk Institute of Science and Technology (DGIST), Daegu 711-873, Republic of Korea*

ARTICLE INFO

ABSTRACT

Semiconductor-based photocatalysts for solar H_2 generation has attracted significant attention because of its great potential for low-cost and clean H_2 production. In this study, we prepared a core–shell structured Au@CdS on TiO$_2$ nanofibers (Au@CdS/TNF) and investigated its photocatalytic H_2 production under visible ($\lambda > 420$ nm) irradiation. Photocatalysts, including Au-deposited CdS/TNF (Au/CdS/TNF) and commercially available TiO$_2$ (P25) instead of TNF, were investigated to determine the effect of a core–shell structured Au@CdS and the role of the TNF. Compared with CdS/TNF and Au/CdS/TNF, the Au@CdS/TNF exhibited strongly enhanced H_2 production under visible irradiation. Furthermore, H_2 production on Au@CdS/TNF was significantly enhanced compared to Au@CdS/P25. These results can be attributed to the synergistic effect of the core–shell structured Au@CdS and the compact structure of TNF. The core–shell structured Au@CdS may inhibit the formation of CdSO$_4$ from CdS and the Au core could transfer electrons from CdS to TiO$_2$ without any screening effect for light absorption by CdS. Moreover, interparticle electron transfer is more favorable for TNF than P25 due to the well-aligned TNF framework. This work demonstrates the synergistic effects of TiO$_2$-based photocatalysts for the improvement of solar H_2 production efficiency.

© 2014 Elsevier B.V. All rights reserved.

1. Introduction

Because H_2 is an environmentally clean fuel, solar H_2 production by semiconductor-based photocatalysis enables achieve a sustainable energy source [1–3]. The most promising semiconductor is TiO$_2$; however, the wide band gap of TiO$_2$ limits the spectrum of solar light that can be utilized. CdS photocatalyst has attracted increasing attention because of its suitable E$_g$, ~2.3 eV, and solar absorption spectrum extending to ~550 nm. Additionally, the conduction band (CB) level of CdS is suitable for H_2 evolution [4]. The photocatalytic efficiency of CdS is highly dependent on various physicochemical properties such as crystallinity (e.g., cubic vs. hexagonal) related to the annealing temperatures used and particle size affecting band gap energy (quantum size effect) and electron donors [5]. Recently, significant progress in solar H_2 production with CdS-based hybrid photocatalysts, including binary (CdS/TiO$_2$,

CdS/ZnO, and CdS/CNT) and ternary materials (CdS/TiO$_2$/Pt), has been demonstrated [6–10].

In general, a cocatalyst is used for photocatalytic H_2 production to increase the overall efficiency by reducing the recombination of photogenerated electrons and holes in the photocatalyst [11]. Noble metals (Pt, Ag, Au) [7,12] and carbon materials (CNT, reduced graphene oxide) [13–15] are used as cocatalysts. On the other hand, the location of the cocatalyst also determines the overall efficiency of H_2 production. Park et al. suggested that the direct particle-to-particle contact of CdS and TiO$_2$ is required to achieve a potential gradient. Therefore, the Pt particle acting as a cocatalyst should be located on the TiO$_2$ particle surface for vectorial electron transfer (CdS $\rightarrow$ TiO$_2$ $\rightarrow$ Pt) [16]. Daskalaki et al. [17] and Strataki et al. [18] suggested that the spatial separation of Pt from CdS/TiO$_2$ is useful for the efficient electron–hole separation. Fang et al. recently reported the importance of the location of Au particles in the CdS-TiO$_2$-Au system, which builds up a transfer path for photogenerated electrons from the CdS to the Au particles via a TiO$_2$ bridge. In addition, they suggested a new type of Au@TiO$_2$-CdS ternary nanostructure [19]. Furthermore, noble metal cocatalysts (such as Au and Ag) act as sensitizers because of their strong surface plasmon resonance absorption, which is commonly used for band gap

* Corresponding author. Tel.: +82 53 785 3410; fax: +82 53 785 3439.
** Corresponding author. Tel.: +82 53 785 6417; fax: +82 53 785 6409.
E-mail addresses: sh2358@dgist.ac.kr (S. Kim), insuil@dgist.ac.kr (S.-I. In).
[1] Both authors contributed equally to this work.

tuning of semiconductor photocatalysts to enhance the photocatalytic activity [20]. Xie et al. reported that cosensitization of Ag and CdS nanoparticles on TiO$_2$ nanotubes produced enhanced photoelectrochemical properties by extending absorption in the visible region, even though the sensitizing effect of Ag is not strong [21]. Zhang et al. also reported that plasmonic hot electrons generated in the Au nanoparticles exhibited enhanced photoelectrochemical water splitting [22].

Several researchers reported that the core–shell structured metal–semiconductor is an efficient visible-light plasmonic photocatalyst, which allows for tunable light absorption over the entire visible-light region by tailoring the shell thickness [23–26]. Following the report by Tada et al. of a CdS-Au-TiO$_2$ system exhibiting enhanced photocatalytic activity by a Z-scheme mechanism [27], hemispherical core–shell-type nanoparticles on various types of TiO$_2$ supports were actively investigated [28–31]. A Z-scheme photocatalyst is composed of successive two-step excitation systems, namely photosystems I and II (PSI, PSII) [32,33]. Tada et al. reported that in the CdS-Au-TiO$_2$ system, CdS, Au, and TiO$_2$ act as the PSI, electron transfer system, and PSII, respectively [27]. CdS-TiO$_2$-Au also showed enhanced photocatalytic activity without the Au-CdS core–shell type [34]. Therefore, further investigations are required concerning the role of the Au core in the core–shell structured Au@CdS, because the reported role of Au deposited on the surface of the CdS-Au is inconsistent.

Another approach to enhance the performance of the TiO$_2$-based photocatalytic system is to align the TiO$_2$ particles into a three-dimensional network [35]. Previously, we reported a well-aligned TiO$_2$ nanoparticle framework, which effectively separated charge pairs and facilitated the charge transfer [36]. The electron transfer mechanisms of this geometric configuration were favorable even for the sensitized system under visible light irradiation [37]. We demonstrated that directionally aligned TiO$_2$ nanofibers (TNFs) obtained via a simple electrospinning method exhibit significantly enhanced activity in terms of H$_2$ production from water under visible light ($\lambda > 420$ nm). Therefore, TNFs have great potential for application to solar H$_2$ production.

In this study, we prepared the core–shell structured Au@CdS on TNF (Au@CdS/TNF) and investigated its photocatalytic H$_2$ production under visible irradiation. To determine the effects of the core–shell structured Au@CdS and the role of TNF, Au-deposited CdS/TNF (Au/CdS/TNF) and commercially available TiO$_2$ (P25), instead of TNF, were employed. Various surface analyses and photoelectrochemical studies were performed to understand the enhanced photocatalytic behavior of Au@CdS/TNF.

2. Experimental

2.1. Materials

Polyvinylpyrrolidone (PVP, M_n 1,300,000), titanium butoxide (Ti(OBu)$_4$), gold(III) chloride hydrate (HAuCl$_4$·xH$_2$O), TiO$_2$ nanoparticles (Degussa, P25), sulfur (S$_8$), cadmium nitrate hexahydrate (Cd(NO$_3$)$_2$·6H$_2$O), sodium sulfide pentahydrate (Na$_2$S·5H$_2$O), and sodium sulfate (Na$_2$SO$_3$) were purchased from Sigma–Aldrich. Ethanol (<99.99%) and methanol (<99.90%) were purchased from J.T. Braker, and deionized water (DI, resistivity > 18 μm) was used throughout the experiments.

2.2. Synthesis of TiO$_2$ nanofibers by electrospinning

TNF was synthesized by the electrospinning method, as previously reported [38]. A polymer solution was prepared by dissolving 0.6 g of PVP in ethanol (10 mL) with vigorous stirring for 24 h. After the polymer was completely dissolved, Ti(OBu)$_4$ (0.5 mM)

was added and the mixture was stirred for an additional 8 h. This homogeneous TiO$_2$ precursor solution was fed at a constant flow rate (15 μL/min) by a constant electric field (20 kV) to obtain dense Ti(OBu)$_4$/PVP nanofiber webs. The distance between the anode (25 gauge stainless steel nozzle) and cathode (collector) was 15 cm. Finally, the Ti(OBu)$_4$/PVP nanofiber webs were calcinated at 550 °C in air for 1 h to remove the PVP polymer and to obtain highly crystalline TNF.

2.3. Photodeposition of Au nanoparticles on TNF

Au nanoparticles were deposited on the surface of TNF (Au/TNF) by photodeposition. The Au precursor was prepared by mixing a 1-mM HAuCl$_4$·xH$_2$O aqueous solution (450 mL) with methanol (50 mL) (as an electron donor). TNF (1 g/L) was added into the Au precursor solution and stirred for 30 min. The mixed solution was then irradiated with a 450-W medium-pressure Hg lamp for 30 min. In order to investigations of the effects of Au particles, Au particles were deposited for 5 min. The samples were filtered, washed, and then dried in an oven at 80 °C for 12 h.

2.4. Decorating the CdS shell on Au/TNF

The CdS shell layer was selectively synthesized by photodeposition on the surface of the Au-TNF. Au-TNF (1 g) was stirred in absolute ethanol (550 mL); then, S$_8$ (0.334 mmol) and Cd(NO$_3$)$_2$·6H$_2$O (3.46 mmol) were added, and nitrogen gas was bubbled through the suspension for 30 min. The mixture was then irradiated with a 450-W medium-pressure Hg lamp for 2 h. After irradiation, the suspension solution was filtered, washed with absolute ethanol, and dried in an oven at 80 °C for 12 h [27].

2.5. Characterization

Morphological images of the surface and transmission electron micrographs were obtained using a field emission scanning electron microscope (FE-SEM, Hitachi SU8020) and a high-resolution transmission electron microscope (HR-TEM, Hitachi HF-3300, operating at 300 kV) equipped with an energy dispersive spectrometer (EDX). X-ray diffraction (XRD) patterns were obtained with an X-ray diffractometer (PANalytical Empyrean, 60 kV) using Cu-Kα_1 radiation ($\lambda = 1.54178$ Å) and a quartz monochromator. Diffused reflection spectroscopy (DRS) was performed using an UV/Visible/NIR spectrometer (Perkin-Elmer Lambda 750) with the wavelength range 300–700 nm. Photoluminescence spectra were measured with a 325-nm He-Cd laser (Kimon, 1 K, 50 mW). Raman spectra were obtained with a Raman spectrophotometer (Thermo Scientific, Nicolet Almega XR) in the wavelength range 100–4000 cm^{-1} using a 325-nm laser. The oxidation states of the Ti, O, Au, Cd, and S atoms were determined by X-ray photoelectron spectroscopy (XPS, Thermo Scientific Escalab 250Xi) using the Mg-Kα line (1253.6 eV) as the excitation source. All binding energies were calibrated from C 1s at 284.6 eV.

2.6. Photocatalytic H$_2$ production and photocurrent measurement

The photocatalytic H$_2$ production experiment was performed by dispersing the photocatalyst (1 g/L) in a distilled water solution of two sacrificial reagents ([Na$_2$S] = [Na$_2$SO$_3$] = 0.1 M). A rectangular quartz reactor (volume: 4 mL) was modified to a head volume of 2.4 mL for analysis using the UV–visible spectrophotometer. A 300-W Xe arc lamp (Newport) with a 420-nm cutoff filter was placed 15 cm from the quartz reactor and N$_2$ gas was bubbled through the photocatalyst suspension for 30 min before irradiation. The produced H$_2$ in the reaction was detected every 30 min for 3 h using a
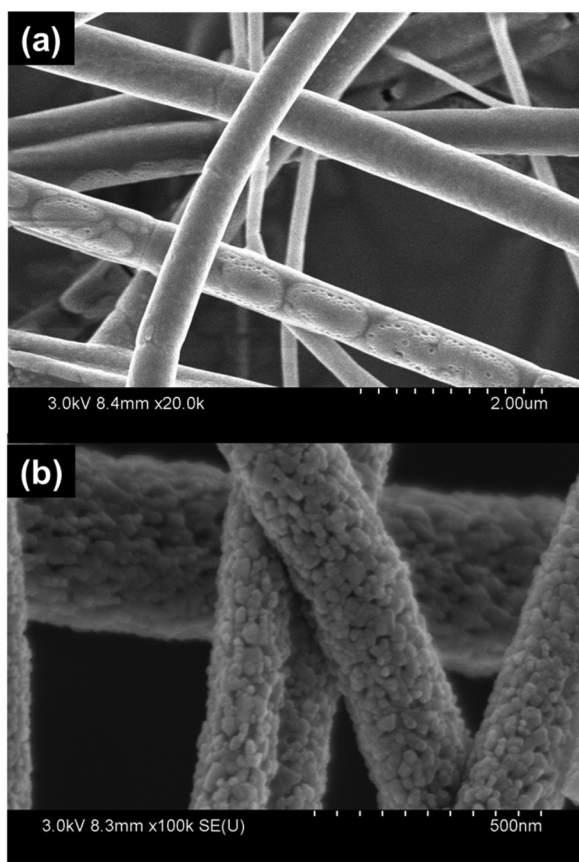
Fig. 1. SEM images of (a) Ti(OBu)$_4$/PVP nanofiber and (b) TNF.

gas chromatograph (GC, Agilent HP6890) equipped with a thermal conductivity detector (TCD).

The photocurrent generated was measured by two types of three-electrode system. One is consisting of an Ag/AgCl electrode, Pt wire, and graphite rod as the reference, working electrode, and counter electrode, respectively. Methyl viologen (MV^{2+}, 0.5 mM) was added to the suspension of the photocatalyst (0.5 g/L, 0.95N NaOH), which is an electron transfer mediator, as described elsewhere [7,13,14,16]. The other is used for the samples coated on conducting FTO glass with electrolyte (Na$_2$SO$_3$ 1 M; pH 9.8). The counter electrode, reference electrode and working electrode are Pt wire electrode, Ag/AgCl and samples/FTO substrate, respectively. Sample/FTO was synthesized by doctor blade methods as describes elsewhere. Briefly, Sample (10 g/0.2 mL) was mixed with polyethylene glycol solution in the mortar. Then it was pasted on the FTO glass (2.5 cm × 1 cm) with 0.48 μm thickness using one layer of 3 M type. Sample/FTO was annealed at 500 °C for 30 min under atmospheric condition then cooled down. A constant voltage (0.45 V vs. Ag/AgCl) was applied to the working electrode using a potentiostat (VSP, Princeton Applied Research). The photocurrent was measured under visible light irradiation (λ > 420 nm) with a constant purge of N$_2$ gas.

3. Results and discussion

3.1. Characterizations of CdS-Au-TNF

Fig. 1 shows the SEM images of the Ti(OBu)$_4$/PVP nanofibers and TNF. The Ti(OBu)$_4$/PVP nanofibers (approximate diameter = 500 nm) have smooth surfaces, whereas the TNF (approximate diameter = 200 nm) consist of a rough surface with porous nanoparticles. Calcination of the nanofiber webs at 550 °C in air for 1 h

effectively removed the PVP to produce highly crystalline TiO$_2$ nanoparticles. Individual nanofibers were densely packed with nanoparticles having a primary particle size of tens of nanometers. While the nanoparticle components are very similar to P25 (see Fig. S1), the morphology of the densely packed TNFs is different from the randomly agglomerated nanoparticles in P25.

Fig. 2 shows the HR-TEM images of Au/TNF, Au@CdS/TNF, and Au/CdS/TNF. In Au-TNF, the Au nanoparticles (10–20 nm) are uniformly deposited on the surface of the TNF with a lattice spacing of 0.232 nm, which corresponds to the (1 1 1) plane (JCPDS 01-1174). The HR-TEM images of Au@CdS/TNF in Fig. 2c and d confirm the formation of a uniform CdS layer on the Au surface, with the previously described CdS shell formations [27]. The reduction of S$_8$ to S^{2-} ions occurred selectively on the Au surface because of the high affinity of Au surface atoms for sulfur. Therefore, S^{2-} ions produced on the Au surface bonded with the Cd^{2+} ions to form a 4-nm-thick CdS shell on the Au surface. The lattice fringes of individual Au and CdS atoms reveals a lattice spacing of 0.232 and 0.375 nm, which corresponds to the (1 1 1) plane of Au (JCPDS 01-1174) and the hexagonal (1 0 0) plane of CdS (JCPDS 65-3414), respectively. On the other hand, in Au/CdS/TNF (Fig. 2e and f), the Au nanoparticles (2–5 nm) were deposited on the CdS/TNF. The lattice fringes of Au/CdS/TNF revealed similar lattice fringes to those of Au@CdS/TNF. Although the conditions for Au deposition were identical, the individual properties of each support (TNF or CdS/TNF) may influence the morphology of the Au nanoparticles. The morphology of the Au nanoparticles photodeposited on TNF is also different from P25 (Fig. S2). Au nanoparticles are uniformly deposited on the surface of TNF, whereas they are irregularly dispersed on P25.

EDX elemental mapping of Au@CdS/TNF (see Fig. 3a and b) shows that Au and CdS are well dispersed on the surface of the TNF. The EDX elemental spectrum (Fig. 3d) of the selected area in the STEM image (Fig. 3c) found signals related to Au, Cd, S, Ti, and O with atomic percentages of around 14.8%, 41.2%, 36.9%, 3.2%, and 3.9%, respectively. The composition ratio of Cd and S was almost 1:1, which is in agreement with the designated ratio. However, the desired composition ratio of Ti and O was not reached, which may be attributed to complete coverage of the TNF surface with CdS and Au.

The XRD and Raman patterns of Au@CdS/TNF, Au/CdS/TNF, Au/TNF, CdS/TNF, and TNF are shown in Fig. 4. As shown in Fig. 4a, TNF shows the crystalline phase of anatase TiO$_2$ (JCPDS 83-2243), which is similar to the XRD pattern of P25 (Fig. S3). Generally, the crystallinity of TiO$_2$ prepared with the sol–gel method is strongly affected by the calcination temperature. TiO$_2$ calcinated at approximately 550 °C typically produces the anatase phase, while the anatase to rutile phase transformation in pure TiO$_2$ usually occurs within 600–700 °C [37]. For CdS/TNF, all TNF peaks remained unchanged, indicating that the procedure for CdS deposition did not influence the TiO$_2$ phase, and the crystallinity of CdS was not high enough to be detected and differentiated from the anatase peaks. On the other hand, the XRD patterns after Au deposition exhibited the characteristic peaks of face-centered cubic (FCC) Au (JCPDS 01-1174). Interestingly, the intensities of the Au peaks for Au/CdS/TNF are lower than Au/TNF and Au@CdS/TNF. This implies that the crystalline size of the Au nanoparticles deposited on the surface of CdS/TNF is smaller than on the surface of TNF, which is consistent with the HR-TEM images (Fig. 2). Characteristic peaks of CdS at 306 and 604 cm^{-1} in the Raman spectra of CdS/TNF and Au@CdS/TNF (Fig. 4b) confirm the formation and presence of CdS. Raman-active modes for the anatase phase of TiO$_2$ were found in all samples at E$_g$ (143 cm^{-1}), B$_{1g}$ (397 cm^{-1}), B$_{1g}$ + A$_{1g}$ (517 cm^{-1}), and E$_g$ (637 cm^{-1}) [39]. For TNF, additional Raman bands at 234, 447, and 612 cm^{-1} were assigned to the B$_{1g}$, E$_g$, and A$_{1g}$ modes of the rutile phase. For Au/TNF and Au/CdS/TNF, the characteristic Raman peaks may be strongly influenced by Au coverage. The
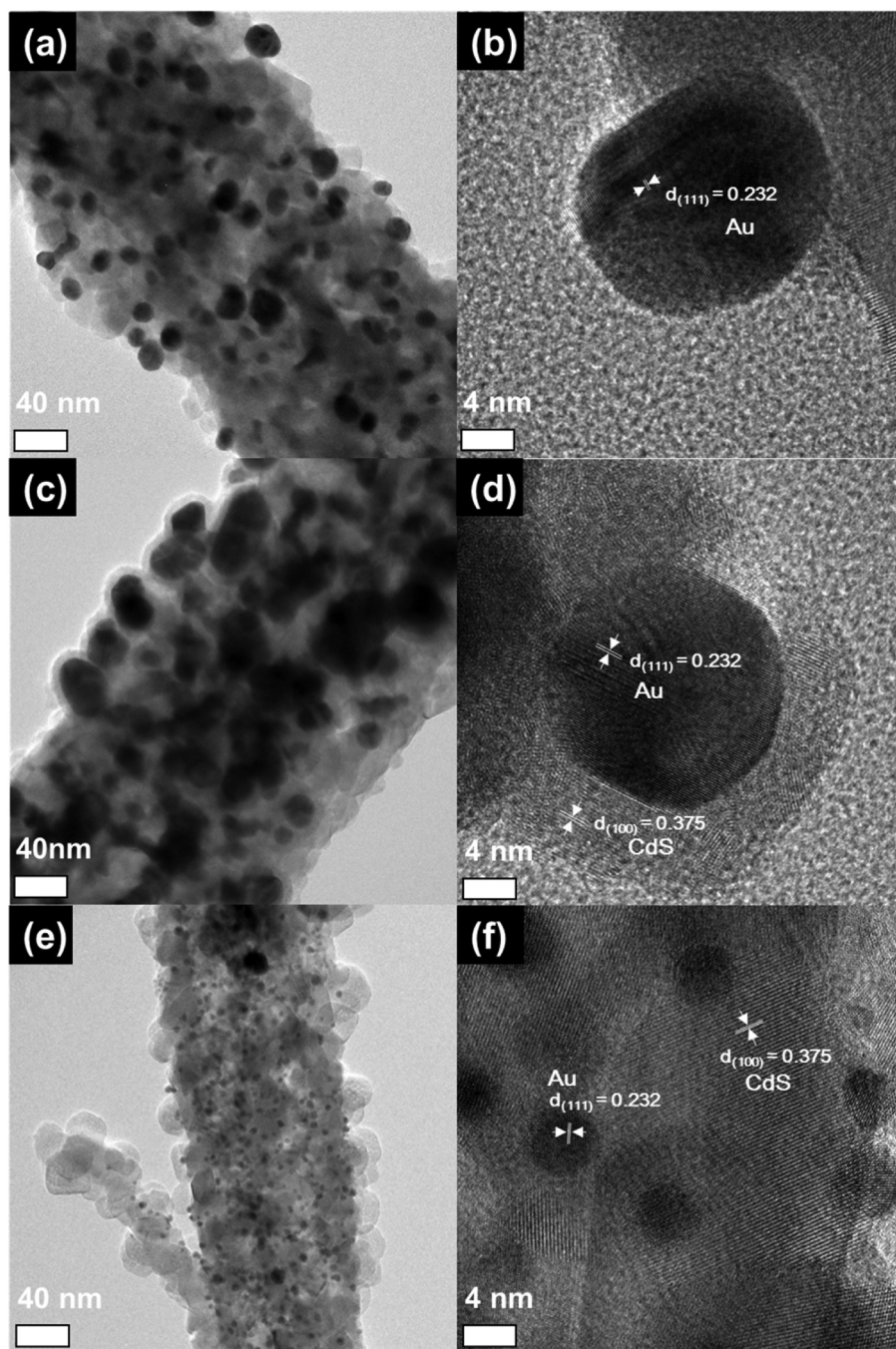
**Fig. 2.** HR-TEM images of (a, b) Au/TNF, (c, d) Au@CdS/TNF, and (e, f) Au/CdS/TNF.

enlarged Raman spectrum of Au/CdS/TNF (Fig. 4b inset) also shows characteristic peaks for CdS and TiO₂.

Fig. 5 shows a comparison of the Ti 2p, Au 4f, Cd 3d, and S 2p XPS spectra of Au@CdS/TNF, Au/CdS/TNF, Au/TNF, CdS/TNF, and TNF. All samples had identical binding energies for Ti $2p_{3/2}$ and Ti $2p_{1/2}$ (458.6 and 464.5 eV, respectively), which could be assigned to the binding energy of TiO₂ (Fig. 5a) [40]. Au 4f peaks were observed for Au/TNF, Au/CdS/TNF, and Au@CdS/TNF. The Au $4f_{7/2}$ and Au $4f_{5/2}$ binding energies of 83.7 and 87.4 eV, respectively, for Au/TNF and Au/CdS/TNF are consistent those of with the metallic state [41]. For Au@CdS/TNF, the Au 4f peak intensity was lower because the Au surface is covered with CdS. The Au $4f_{7/2}$ binding energy is also slightly shifted to a higher binding energy, which may be attributed to the formation of oxidized Au during CdS

deposition. The Cd 3d peaks were also observed in CdS/TNF, Au@CdS/TNF, and Au/CdS/TNF. The binding energies for Cd $3d_{5/2}$ and Cd $3d_{3/2}$ of both CdS/TNF and Au@CdS/TNF are 405.2 and 411.9 eV, respectively. These values are consistent with the binding energies of CdS [7], whereas the Cd 3d peaks of Au/CdS/TNF are slightly shifted to a lower binding energy. This implies that the partially reduced Cd ions from Cd^{2+} could be formed during Au deposition. The S $2p_{1/2}$ and $2p_{3/2}$ peaks appear at 162.4 and 161.2 eV, respectively, supporting CdS formation. Meanwhile, the additional S 2p peak at 168.4 eV was attributed to CdSO₄ [25]. The relative intensities of these peaks (168.4 eV for CdSO₄ and 161.2 eV for CdS) were roughly calculated as 0.75, 0.57, and 0.38 for CdS/TNF, Au/CdS/TNF, and Au@CdS/TNF, respectively. This result implies that the codeposition of Au and CdS could inhibit the formation of CdSO₄
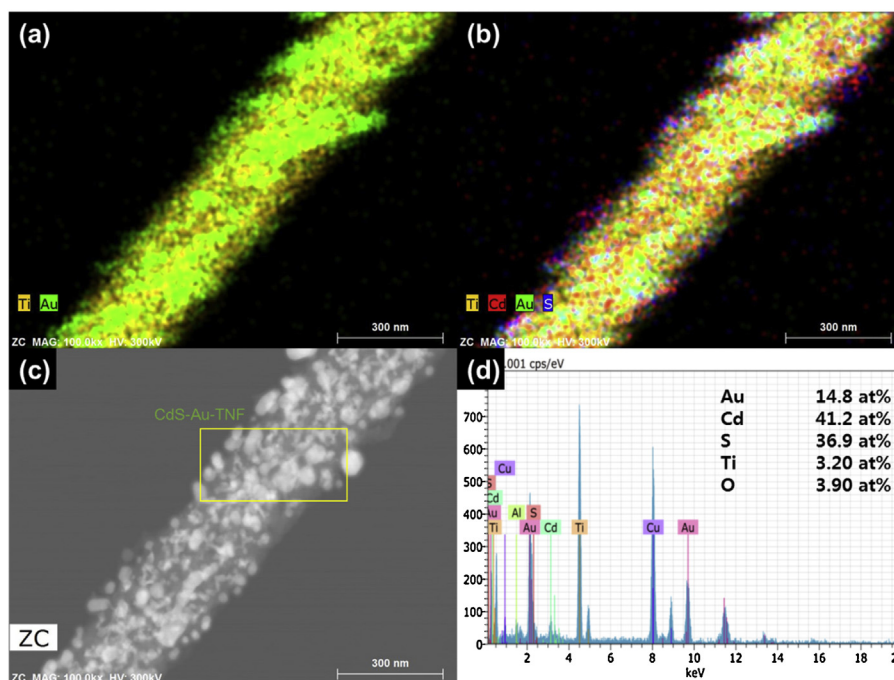
Fig. 3. EDX elemental mapping of Au@CdS/TNF (a) Ti, Au and (b) Ti, Au, Cd, and S mapping. (c) STEM image of Au@CdS/TNF and (d) EDX elemental spectrum and ratio of the selected area shown in (c).
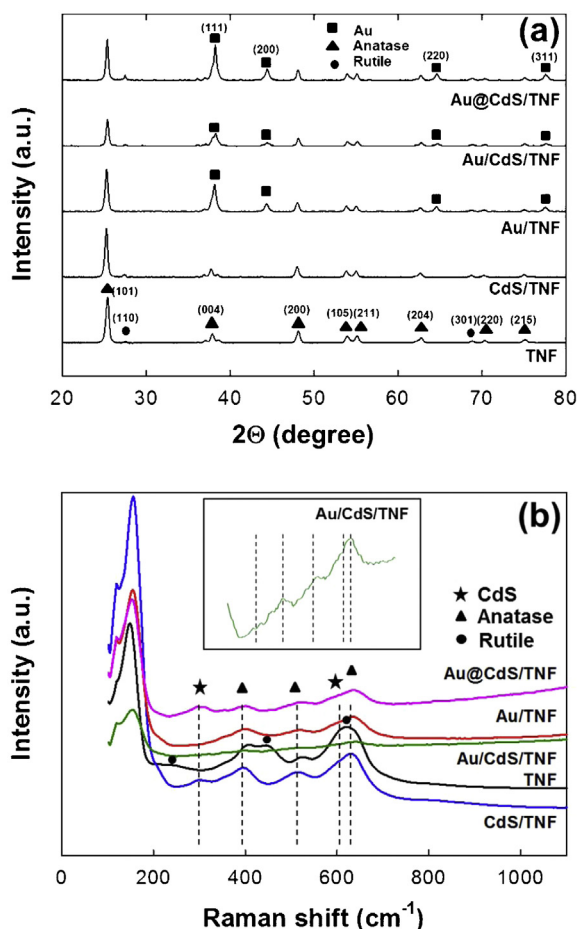
Fig. 4. (a) XRD pattern and (b) Raman spectra of Au@CdS/TNF, Au/CdS/TNF, Au/TNF, CdS/TNF, and TNF. The inset shows an enlargement of the graph for Au/CdS/TNF.

from CdS, thereby increasing the stability of CdS. Therefore, the core–shell structured Au@CdS may be crucial for enhancing the photocatalytic activity of CdS.

To investigate the influence of the core–shell structured Au@CdS on light absorption, the UV–visible absorption spectra of Au@CdS/TNF, Au/CdS/TNF, Au/TNF, CdS/TNF, and TNF were measured (Fig. 6). The high absorption of UV light (~400 nm) for TNF may correspond to the band-edge absorption of TiO_2 [11]. For CdS/TNF, the absorption from 400 to 550 nm may be attributed to the absorption band of the CdS nanoparticles [19]. Compared with TNF, Au/TNF shows a strong absorption band centered at 550 nm, which corresponds to plasmonic resonance absorption of the Au nanoparticles. Plasmon resonance absorption was also found in Au@CdS/TNF and Au/CdS/TNF, which also show a CdS absorption band. However, as previously reported, the absorption peaks are red-shifted because of strong electronic interactions between Au and CdS [27]. Plasmon resonance absorption peaks are also sensitive to the size and shape of the Au nanoparticles and the surrounding environment [24,26]. Chen et al. showed that increasing the CdS shell thickness could cause an increased red-shift in the surface plasmon resonance position of Au [23]. For Au@CdS/TNF, an increased red-shift in the plasmon resonance absorption of Au was observed, which was also found for Au@CdS/P25 (see Fig. S4). These results demonstrate that the core–shell structured Au@CdS was successfully formed on the surface of TNF, and strong interactions between Au and CdS were observed.

3.2. Photocatalytic H_2 production and photocurrent generation

Fig. 7 shows that visible light-induced H_2 production on TNF-based samples compared with P25-based samples. In the absence of CdS, no H_2 was produced. As shown in Fig. 6 and Fig. S4, TNF or P25 alone cannot absorb visible light because their band gaps are too large. However, Au/TNF and Au/P25 did not produce H_2 under visible light irradiation, even though plasmon resonance absorptions at approximately 550 nm were observed for both photocatalysts. Therefore, the plasmonic electrons excited by plasmon resonance absorption of Au may recombine faster than they are extracted
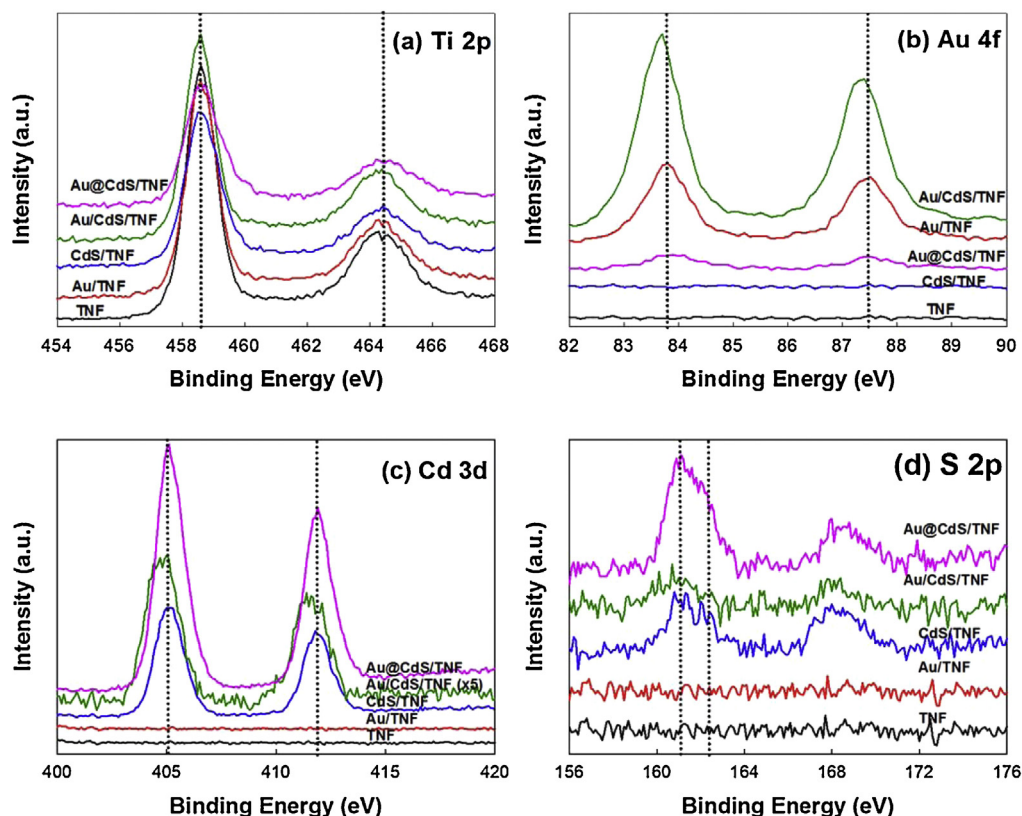
Fig. 5. (a) Ti 2p, (b) Au 4f, (c) Cd 3d, and (d) S 2p peaks in the XPS spectra of Au@CdS/TNF, Au/CdS/TNF, Au/TNF, CdS/TNF, and TNF.
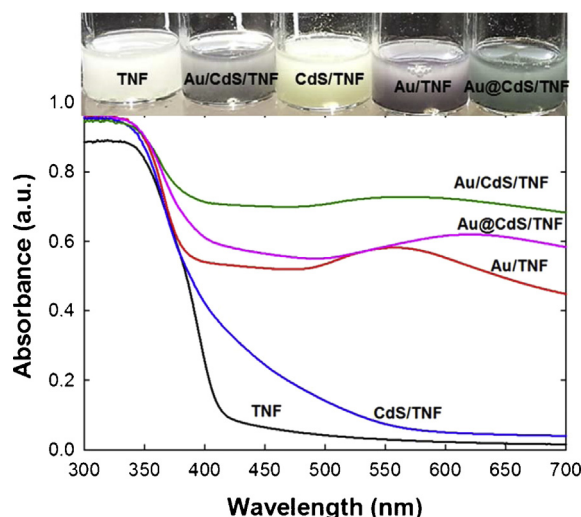

Fig. 6. UV–visible absorption spectra of Au@CdS/TNF, Au/CdS/TNF, Au/TNF, CdS/TNF, and TNF, including photographs of the aqueous suspensions (0.1 wt.%) of Au@CdS/TNF, Au/CdS/TNF, Au/TNF, CdS/TNF, and TNF.

Fig. 7. (a) Time-profiled H_2 production plots of TNF and P25-based photocatalysts under visible ($\lambda > 420$ nm) irradiation. Sacrificial reagents were 0.1 M of [Na_2S] and [Na_2SO_3]. (b) Photographs of the aqueous suspension (0.1 wt.%) and bar graphs of the amount of H_2 evolved after 3 h.

for reaction with electron acceptors. Although the hot electrons and holes produced by plasmon resonance could increase the solar energy conversion efficiency [22], H_2 production by only hot electrons on Au-TiO$_2$ or (N-TiO$_2$) may be negligible, which is consistent with previous results [30]. CdS/TNF and CdS/P25 produced up to 1.7 μmol and 2.0 μmol of H_2, respectively, after 3 h of visible light irradiation, which implies that the morphologies of TiO$_2$ do not have a strong influence on H_2 production. On the other hand, Au deposition on CdS/TNF and CdS/P25 produced a slight reduction in H_2 production. For these cases, the Au nanoparticles on the surface of CdS/TNF or CdS/P25 may function as light-absorption
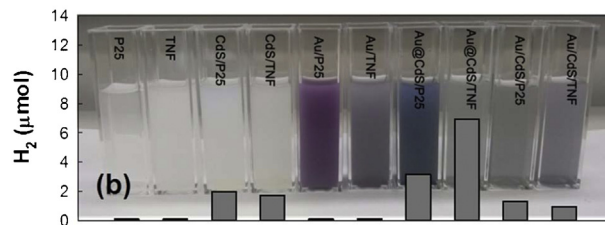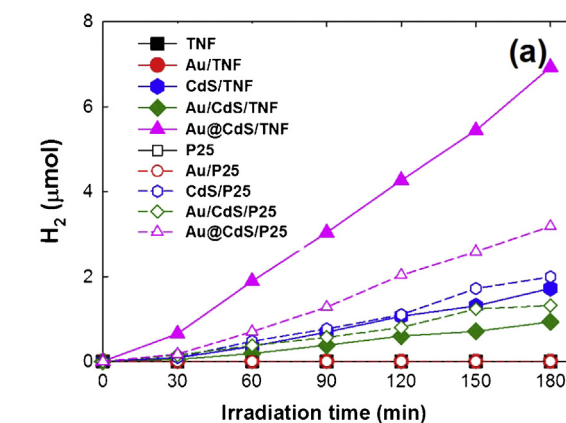
inhibitors as well as an electron relay. Therefore, decrease in H_2 production was the largest effect that the Au nanoparticles produced in both CdS/TNF and CdS/P25. In contrast, both Au@CdS/TNF and Au@CdS/P25 exhibited strongly enhanced H_2 production under
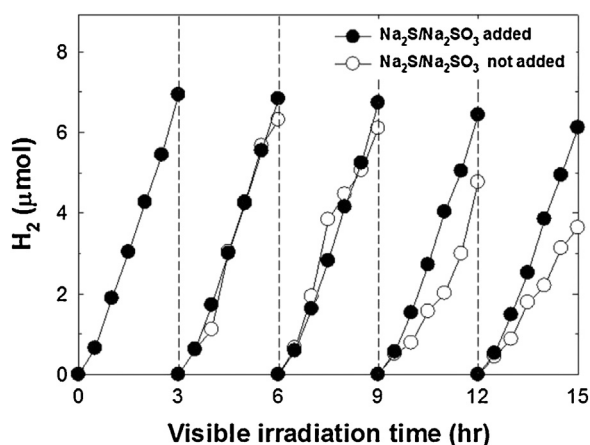
Fig. 8. Repeated runs of the visible ($\lambda > 420$ nm) light induced H_2 production on Au@CdS/TNF. Sacrificial reagents were 0.1 M of [Na_2S] and [Na_2SO_3].

visible irradiation because of the core–shell structure Au@CdS in which the Au nanoparticles function as electron mediators for CdS-to-TNF and CdS-to-P25. In order to compare the samples with the similar Au nanoparticles between Au/CdS/TNF and Au@CdS/TNF, the Au nanoparticles were photodeposited on TNF for 5 min (Au(5)/TNF) and then CdS shell layer was sequentially deposited on Au(5)/TNF, which was designated to Au(5)@CdS/TNF. Fig. S5 shows the TEM images of Au(5)@CdS/TNF and the visible light H_2 production of Au/CdS/TNF, Au(5)@CdS/TNF, and Au@CdS/TNF. For the H_2 production, Au(5)@CdS/TNF was more than three times higher than Au/CdS/TNF even though they have similar size of Au nanoparticles. This result supports that the core–shell structure Au@CdS on TNF was more favorable than Au/CdS on TNF for the visible light induced H_2 production. Moreover, H_2 production on Au@CdS/TNF was more enhanced than on Au@CdS/P25. Previous studies revealed that agglomerated TiO_2 species such as TNF are better for photocatalytic H_2 production, even under visible light irradiation because of the enhanced interparticle electron transfer through the well-aligned TNF framework [35–37]. The core–shell structured Au@CdS could enhance the electron transfer from CdS to TiO_2 (TNF or P25) and then the morphological effects of TiO_2 could be more important. The plasmonic photosensitizing effect of Au may also enhance H_2 production, as previously reported for the Au@CdS/TiO_2 sandwich system [31]. However, enhanced H_2 production by plasmonic sensitization in Au may be less pronounced than changes in the CdS band gap excitation energy, because the irradiated wavelengths were longer than 420 nm. This is consistent with a previous report, which found that enhancing the optical absorption of plasmon-coupled semiconductor materials via electron transfer requires the semiconductor component to be electrically insulated, thus preventing the backward flow of charge into the metal nanoparticles [24]. Therefore, the synergistic effect of the electron relay (Au core) and efficient interparticle electron transfer (in the densely packed TiO_2 nanoparticles) could be responsible for the enhanced photocatalytic H_2 production on Au@CdS/TNF under visible irradiation. To investigate whether or not Au@CdS/TNF becomes deactivated, the visible light induced H_2 production was repeated over five cycles, as shown in Fig. 8. When the sacrificial reagents were not added during all repeated cycles, the H_2 production was decreased during the repeat cycles. However, as the sacrificial reagents were added every repeated cycle, the H_2 production was very slowly decreased. This result indicates that Au@CdS/TNF is somewhat stable and reusable.

The Au@CdS/TiO_2 three-component system is known for Z-scheme mechanisms, in which CdS, TiO_2, and Au are PSI, PSII, and the electron transfer system, respectively [27,28,30]. To investigate
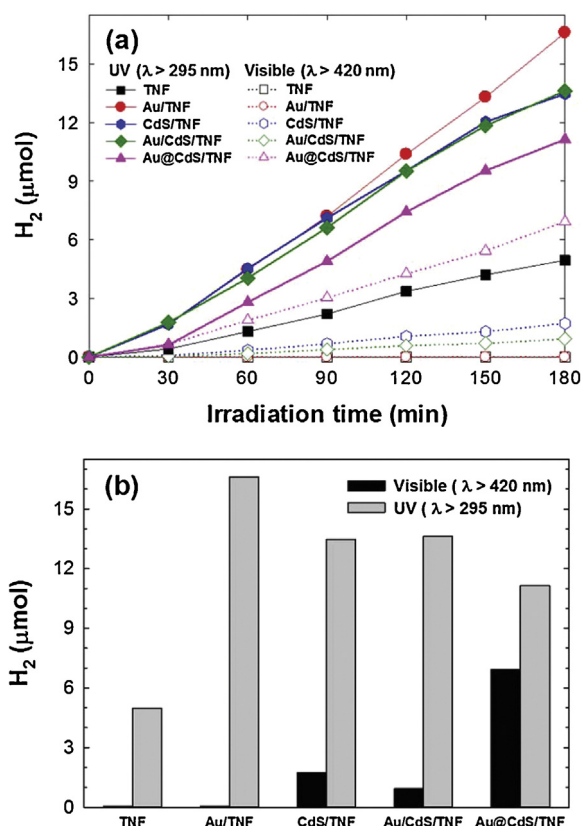

Fig. 9. (a) Time-profiled photocatalytic H_2 evolution under UV ($\lambda > 295$ nm) and visible ($\lambda > 420$ nm) and (b) a summary of the amount of evolved H_2 after 3 h under UV ($\lambda > 295$ nm) and visible ($\lambda > 420$ nm) light irradiation.

the effects of a Z-scheme mechanism for Au@CdS/TNF, the TNF should be activated by band gap excitation. Therefore, the photocatalytic H_2 production was compared under UV ($\lambda > 290$ nm) irradiation, as shown in Fig. 9. In contrast to visible irradiation, Au/TNF exhibited enhanced H_2 production under UV light and the coexistence of CdS on Au did not show any synergistic effect for H_2 production. The core–shell structured Au@CdS on the surface of TNF reduced rather than enhanced H_2 production. Under UV irradiation, the Au core resulted in electron retardation by suppressing the electron–hole pair recombination of TiO_2. Therefore, the Z-scheme mechanism for UV-light-induced H_2 production was not efficient in our Au@CdS/TNF, and the coexistence of CdS on Au/TNF inhibited light absorption by TNF and H_2 production on the surface of Au/TNF.

To confirm the charge separation behavior, PL spectra were measured, and the results are shown in Fig. 10. Au/TNF and Au/CdS/TNF had the lowest PL peak energies, indicating that the Au nanoparticles deposited on TNF and CdS/TNF could reduce the recombination of electron–hole pairs. On the other hand, CdS/TNF showed a higher-energy PL peak than TNF. For CdS/TNF, photoinduced electron transfer from TiO_2 to CdS could not occur because of the higher conduction-band position of CdS than TiO_2. Further increases in the PL peak energy are due to the electron–hole pair recombination of CdS. CdS-Au-TNF also showed increased peak energy in the photoluminescence spectra in the range 400–600 nm, which may be attributed to electron–hole pair recombination in the CdS layer. This implies that in Au@CdS/TNF, some of the excited electrons in the CdS shell are not transferred to the Au core, but remained and recombined in the CdS shell, indicating that H_2 production could occur on the surface of CdS and TiO_2 in Au@CdS/TiO_2.

Photocurrent generation measurements were conducted in a suspension or coating on FTO under visible irradiation. Fig. 11a
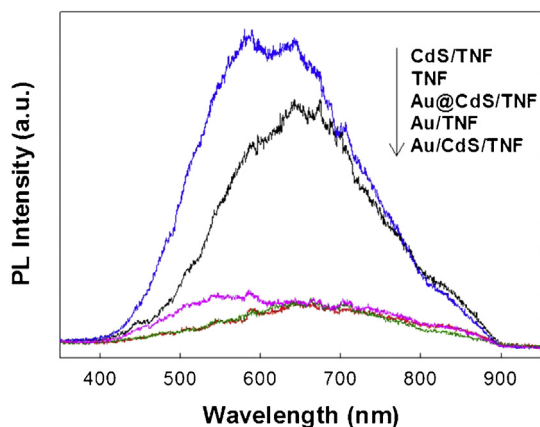
Fig. 10. Photoluminescence spectra (excited at 325 nm) of Au@CdS/TNF, Au/CdS/TNF, Au/TNF, CdS/TNF, and TNF.
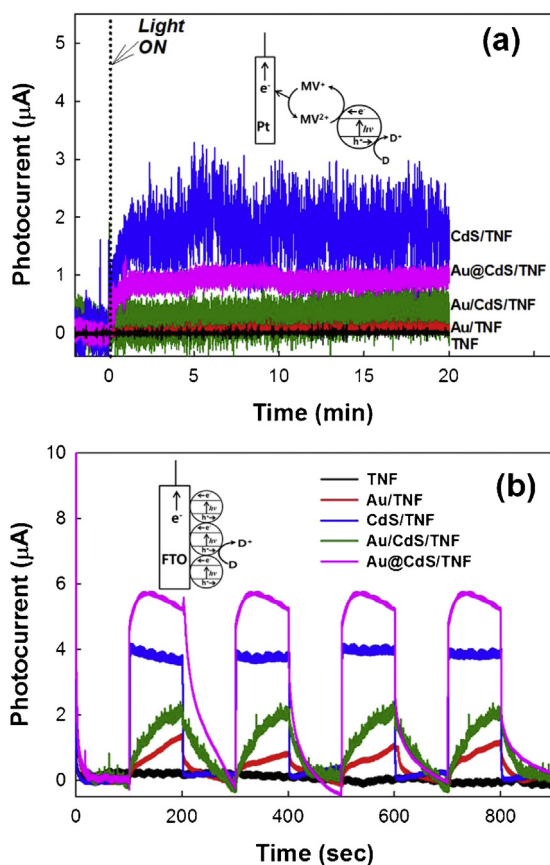

Fig. 11. Time-profiled photocurrent generations under visible (λ > 420 nm, 100 mW/cm²) irradiation. (a) Suspension type: photocatalyst, 0.5 g/L in 0.95 N NaOH; MV^{2+}, 0.5 mM; Pt wire was used as an electron collecting working electrode held at +0.4 V vs. Ag/AgCl. The counter electrode was a graphite rod. (b) Coating type: 1 M Na_2SO_3; pH 9.8. Samples coated FTO electrode was used as a working electrode held at +0.4 V vs. Ag/AgCl. The counter electrode was a Pt wire electrode.

shows the time-profiled photocurrent generation in a suspension including an MV^{2+}/MV^+ couple as an electron shuttle and methanol as an electron donor. As soon as CdS/TNF and Au@CdS/TNF were irradiated under visible light, the photocurrent quickly increased and finally reached a plateau. The Au/CdS/TNF photocatalyst exhibited lower photocurrent generation than CdS/TNF and Au@CdS/TNF. Both TNF and Au/TNF did not show any photocurrent generation because the band gap is too large to utilize visible light. Interestingly, the photocurrent generated by CdS/TNF was higher
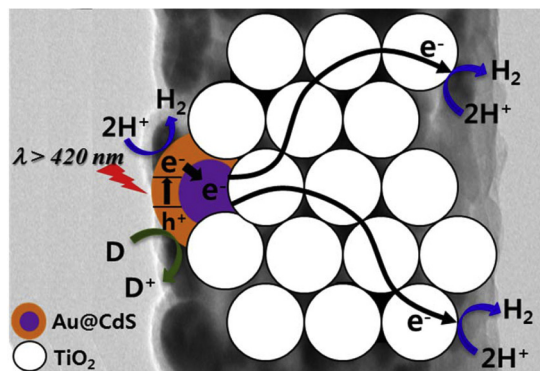

Fig. 12. Schematic illustration of the dominant H_2 evolution mechanism of Au@CdS/TNF under visible light irradiation (λ > 420 nm).

than Au@CdS/TNF. This was attributed to the difference between MV^{2+}-induced photocurrent generation and photocatalytic H_2 production, as previously reported [13]. The MV^{2+}-induced current is generated via single-electron transfer and could proceed relatively efficiently without a cocatalyst. However, H_2 is produced via a two-electron transfer through two consecutive steps (H_2 adsorption and desorption) and requires a catalyst for effective multielectron transfer. Therefore, generation of less photocurrent in Au@CdS/TNF indicates that the Au particles are not effective in catalyzing single-electron transfer, but compete with MV^{2+} for photogenerated electrons. This implies that photogenerated electrons in the CdS shell can transfer to the Au core. On the other hands, Fig. 11b shows that the photocurrent generation of sample/FTO is consistent with the tendency of the H_2 production as shown in Fig. 7a. TNF shows negligible photocurrent whereas Au/TNF and Au/CdS/TNF show the increasing of photocurrent generation, which might be due to the plasmon-assisted enhancement. CdS/TNF and Au@CdS/TNF show the higher photocurrent generation. This result implies that the visible light absorption by CdS at the surface of CdS/TNF and Au@CdS/TNF could be responsible for the photocurrent generation and the Au core efficiently electron transfer from CdS to FTO through TNF.

The mechanism for H_2 production on Au@CdS/TNF, based on the above-discussed results, is explained with the help of Fig. 12. First, the CdS shell absorbs visible light, exciting the electrons in its valence band and producing electrons in the conduction band and holes in the valence band of the CdS shell. The holes then react with an electron donor at the surface of the CdS shell and the electrons transfer either to the Au core or react directly with H^+ to produce H_2. The electrons transferred to the Au core are subsequently transferred to the TNF, followed by interparticle electron transfer through the densely packed TNF and finally react with H^+ to produce H_2. The core–shell structured Au@CdS and the densely packed TiO_2 nanoparticles could be responsible for enhanced photocatalytic H_2 production on Au@CdS/TNF under visible irradiation.

4. Conclusion

The core–shell structured Au@CdS deposited on TNF was prepared and its photocatalytic H_2 production under visible light was investigated. First, 10–20 nm-sized Au nanoparticles were uniformly deposited on the surface of TNF with approximate diameters of 500 nm. Second, uniform CdS shells with thickness 4 nm were coated on the surface of the Au core. Compared with CdS/TNF and Au/CdS/TNF, the Au@CdS/TNF exhibited strongly enhanced H_2 production under visible irradiation. This enhancement resulted from the synergistic effects of the core–shell structured Au@CdS and densely packed TiO_2 nanoparticles. The core–shell structured

Au@CdS may inhibit the formation of CdSO$_4$ from CdS and the Au core could transfer electrons from CdS to TiO$_2$ without any screening effect for light absorption by CdS. The drastic enhancement of H$_2$ production on Au@CdS/TNF compared to Au@CdS/P25 implies that TNF is more favorable for photocatalytic H$_2$ production than P25 for the visible light-irradiated sensitization mechanism. Therefore, these synergistic modifications are useful for improve the solar H$_2$ production of TiO$_2$-based photocatalysts.

Acknowledgments

Appendix A. Supplementary data

Supplementary data associated with this article can be found, in the online version, at http://dx.doi.org/10.1016/j.apcatb.2014.11.036.

References

[1] X.B. Chen, S.H. Shen, L.J. Guo, S.S. Mao, Chem. Rev. 110 (2010) 6503–6570.
[2] P.V. Kamat, J. Bisquert, J. Phys. Chem. C 117 (2013) 14873–14875.
[3] H.L. Zhou, Y.Q. Qu, T. Zeid, X.F. Duan, Energy Environ. Sci. 5 (2012) 6732–6743.
[4] M. Matsumura, Y. Saho, H. Tsubomura, J. Phys. Chem. 87 (1983) 3807–3808.
[5] D.W. Jing, L.J. Guo, J. Phys. Chem. B 110 (2006) 11139–11145.
[6] W.-T. Sun, Y. Yu, H.-Y. Pan, X.-F. Gao, Q. Chen, L.-M. Peng, J. Am. Chem. Soc. 130 (2008) 1124.
[7] Y.K. Kim, H. Park, Energy Environ. Sci. 4 (2011) 685–694.
[8] H. Park, Y.K. Kirn, W. Choi, J. Phys. Chem. C 115 (2011) 6141–6148.
[9] E. Rabinovich, G. Hodes, J. Phys. Chem. C 117 (2013) 1611–1620.
[10] T.Y. Peng, P. Zeng, D.N. Ke, X.J. Liu, X.H. Zhang, Energy Fuels 25 (2011) 2203–2210.
[11] H. Park, Y. Park, W. Kim, W. Choi, J. Photochem. Photobiol. C-Photochem. Rev. 15 (2013) 1–20.
[12] V. Jovic, W.-T. Chen, D. Sun-Waterhouse, M.G. Blackford, H. Idriss, G.I.N. Waterhouse, J. Catal. 305 (2013) 307–317.
[13] G. Khan, S.K. Choi, S. Kim, S.K. Lim, J.S. Jang, H. Park, Appl. Catal. B-Environ. 142 (2013) 647–653.
[14] H.W. Jeong, H. Park, Catal. Today 230 (2014) 15–19.
[15] H.I. Kim, S. Kim, J.K. Kang, W. Choi, J. Catal. 309 (2014) 49–57.
[16] H. Park, W. Choi, M.R. Hoffmann, J. Mater. Chem. 18 (2008) 2379–2385.
[17] V.M. Daskalaki, M. Antoniadou, G.L. Puma, D.I. Kondarides, P. Lianos, Environ. Sci. Technol. 44 (2010) 7200–7205.
[18] N. Strataki, M. Antoniadou, V. Dracopoulos, P. Lianos, Catal. Today 151 (2010) 53–57.
[19] J. Fang, L. Xu, Z.Y. Zhang, Y.P. Yuan, S.W. Cao, Z. Wang, L.S. Yin, Y.S. Liao, C. Xue, ACS Appl. Mater. Interfaces 5 (2013) 8088–8092.
[20] S. Zeng, K.-T. Yong, I. Roy, X.-Q. Dinh, X. Yu, F. Luan, Plasmonics 6 (2011) 491–506.
[21] K.P. Xie, Q. Wu, Y.Y. Wang, W.X. Guo, M.Y. Wang, L. Sun, C.J. Lin, Electrochem. Commun. 13 (2011) 1469–1472.
[22] X. Zhang, Y. Liu, S.T. Lee, S.H. Yang, Z.H. Kang, Energy Environ. Sci. 7 (2014) 1409–1419.
[23] W.T. Chen, T.T. Yang, Y.J. Hsu, Chem. Mat. 20 (2008) 7204–7206.
[24] S. Lambright, E. Butaeva, N. Razgoniaeva, T. Hopkins, B. Smith, D. Perera, J. Corbin, E. Khon, R. Thomas, P. Moroz, A. Mereshchenko, A. Tarnovsky, M. Zamkov, ACS Nano 8 (2014) 352–361.
[25] T.T. Yang, W.T. Chen, Y.J. Hsu, K.H. Wei, T.Y. Lin, T.W. Lin, J. Phys. Chem. C 114 (2010) 11414–11420.
[26] J.T. Li, S.K. Cushing, J. Bright, F.K. Meng, T.R. Senty, P. Zheng, A.D. Bristow, N.Q. Wu, ACS Catal. 3 (2013) 47–51.
[27] H. Tada, T. Mitsui, T. Kiyonaga, T. Akita, K. Tanaka, Nat. Mater. 5 (2006) 782–786.
[28] H.M. Zhu, B.F. Yang, J. Xu, Z.P. Fu, M.W. Wen, T. Guo, S.Q. Fu, J. Zuo, S.Y. Zhang, Appl. Catal. B-Environ. 90 (2009) 463–469.
[29] L. Ding, H. Zhou, S. Lou, J. Ding, D. Zhang, H.X. Zhu, T.X. Fan, Int. J. Hydrog. Energy 38 (2013) 8244–8253.
[30] H. Zhou, L. Ding, T.X. Fan, J. Ding, D. Zhang, Q.X. Guo, Appl. Catal. B-Environ. 147 (2014) 221–228.
[31] J. Li, S.K. Cushing, P. Zheng, T. Senty, F. Meng, A.D. Bristow, A. Manivannan, N. Wu, J. Am. Chem. Soc. 136 (2014) 8438–8449.
[32] J.F. Allen, W. Martin, Nature 445 (2007) 610–612.
[33] K. Maeda, ACS Catal. 3 (2013) 1486–1503.
[34] T. Lv, L.K. Pan, X.J. Liu, Z. Sun, Electrochim. Acta 83 (2012) 216–220.
[35] N. Lakshminarasimhan, A.D. Bokare, W. Choi, J. Phys. Chem. C 116 (2012) 17531–17539.
[36] S.K. Choi, S. Kim, S.K. Lim, H. Park, J. Phys. Chem. C 114 (2010) 16475–16480.
[37] S.K. Choi, S. Kim, J. Ryu, S.K. Lim, H. Park, Photochem. Photobiol. Sci. 11 (2012) 1437–1444.
[38] D. Li, Y.N. Xia, Nano Lett. 3 (2003) 555–560.
[39] G. Liu, H.G. Yang, C. Sun, L. Cheng, L. Wang, G.Q. Lu, H.-M. Cheng, CrystEngComm 11 (2009) 2677–2682.
[40] S. Kim, M. Kim, Y.K. Kim, S.H. Hwang, S.K. Lim, Appl. Catal. B-Environ. 148 (2014) 170–176.
[41] S. Axnanda, M. Scheele, E. Crumlin, B.H. Mao, R. Chang, S. Rani, M. Faiz, S.D. Wang, A.P. Alivisatos, Z. Liu, Nano Lett. 13 (2013) 6176–6182.